PHYSICAL REVIEW B **88**, 094108 (2013)

Thermodynamics of the Zr-O system from first-principles calculations

B. Puchala[1,*] and A. Van der Ven[1,2,†]

[1]*Department of Materials Science and Engineering, University of Michigan, Ann Arbor, Michigan 48109, USA*

[2]*Materials Department, University of California, Santa Barbara, California 93106, USA*

(Received 16 May 2013; published 30 September 2013)

We investigate the electronic and thermodynamic properties of Zr and its oxides from first principles to elucidate phase stability in the Zr-O system. Hexagonally close-packed Zr is unusual in its ability to dissolve very high concentrations of oxygen over its interstitial octahedral sites, forming a variety of ordered suboxides that undergo both first-order and second-order phase transitions upon heating. We perform a first-principles, statistical-mechanical analysis of finite temperature phase stability of ZrO_x using a cluster expansion Hamiltonian and Monte Carlo calculations. This analysis predicts the existence of 0-K ground-state oxygen orderings at composition $ZrO_{1/6}$, $ZrO_{2/9}$, $ZrO_{1/3}$, $ZrO_{4/9}$, and $ZrO_{1/2}$ along with evidence of an infinite sequence of ground-state suboxide orderings at intermediate oxygen concentrations consisting of different stackings of empty, $\frac{1}{3}$-filled and $\frac{2}{3}$-filled two-dimensional oxygen layers. We also predict the stability of a previously uncharacterized Zr-monoxide phase, which we label δ'-ZrO due to its crystallographic relation to δ-TiO. The δ'-ZrO structure is equivalent to the high-pressure ω-Zr phase but has interstitial oxygen ordering. Finally, as part of the technical implementation of our statistical mechanical study, we introduce a new algorithm to parametrize the coefficients of a cluster expansion Hamiltonian and apply a k-space analysis to rigorously track order-disorder phenomena at finite temperature.

DOI: 10.1103/PhysRevB.88.094108 PACS number(s): 61.50.Ah, 64.70.K−, 81.30.Bx, 71.20.Be

I. INTRODUCTION

Controlling the growth and properties of zirconium oxide is important to a wide range of technologies. Zirconium alloys are used in high-temperature applications such as nuclear fuel rod cladding due to their excellent corrosion resistance, a low-absorption cross-section for neutrons, high hardness, and ductility. ZrO_2, particularly when stabilized in the cubic form by alloying with Y_2O_3, is used as a solid oxide fuel cell (SOFC) electrolyte and for thermal barrier coatings. Thin films of ZrO_2 show promise as a high-κ dielectric for microelectronics. Of significant interest for any of these applications is a predictive theory of Zr oxidation. Since oxidation involves the formation of new phases, atomic diffusion, and electronic transport,[1] any attempt to rationalize and predict this process requires a thorough characterization of the thermodynamic, kinetic, and electronic properties of the Zr-O system.

A remarkable property of Zr is its high oxygen solubility limit. In contrast to most other elemental metals, Zr can dissolve oxygen up to as much as 35 at% (for the experimental phase diagram see Ref. 2). Addition of more oxygen results in the transformation to ZrO_2, which, depending on the temperature, can exist in three polymorphs at standard pressure. A cubic form, γ-ZrO_2, is stable at high temperature and has the fluorite structure. The Zr atoms of γ-ZrO_2 form a face-centered cubic (fcc) sublattice with oxygen occupying the tetrahedral interstitial positions of the Zr sublattice. At lower temperatures, tetragonal and monoclinic distortions of the cubic phase become stable. For stoichiometric ZrO_2, the cubic phase transforms to tetragonal β-ZrO_2 at 2650 K, while the tetragonal form transforms to moniclinic α-ZrO_2 at 1478 K. In contrast to β- and α-ZrO_2, cubic γ-ZrO_2 is able to accommodate significant oxygen understoichiometry ($0 \leqslant x \leqslant 0.44$ in γ-ZrO_{2-x}), rendering it stable to temperatures as low as 1798 K at understoichiometric compositions. In addition to γ-, β-, and α-ZrO_2, at least two orthorhombic phases are stabilized at high pressure.[3]

Pure Zr is stable in the hcp crystal structure (α-Zr) at low to intermediate temperature and transforms to the bcc crystal structure (β-Zr) above 1163 K.[2] Both hcp and bcc polymorphs of Zr are able to dissolve high concentrations of oxygen. The oxygen solubility of β-Zr reaches as high as 10.5 at% oxygen at high temperatures, while the maximum solubility of α-Zr reaches values as high as 28.6–35 at% oxygen. Oxygen is known to occupy octahedral interstitial positions in α-Zr. At low temperatures and high oxygen content, oxygen ordering over the octahedral sites of hcp Zr has been observed experimentally with neutron and x-ray diffraction. Similar oxygen solubility and ordering is observed in titanium[4] and hafnium.[5] Phase transformations between the various orderings have been observed by calorimetry and electrical resistivity measurements. While boundaries between ordered phases have been determined[2,6,7] they are considered speculative because of the difficulty of equilibrating at low temperatures. In addition to α- and β-Zr, hexagonal ω-Zr with an AlB_2 type crystal structure is stable in the pressure range ~2–35 GPa.[8]

Several *ab initio* studies of the various polymorphs of Zr and ZrO_2 have been performed to elucidate their electronic, structural, and vibrational properties (see Refs. 8–10 and those cited within), with a particular emphasis on understanding the transformations between the various phases. Oxygen dissolution in α-Zr was recently investigated by Ruban *et al.*[11] who used a pair-interaction Hamiltonian, parameterized using *ab initio* calculations at dilute oxygen concentrations, to predict the stability of oxygen ordering at $ZrO_{1/3}$ and $ZrO_{1/2}$. More recently, Burton *et al.*[12] calculated a Zr-O phase diagram from first-principles calculations for the concentration range $0 \leqslant x \leqslant 0.5$ in ZrO_x. They identified $ZrO_{1/6}$, $ZrO_{1/3}$, $ZrO_{5/12}$,

and $ZrO_{1/2}$ as 0-K ground states. Their cluster expansion did not predict long-period superstructure O orderings, in contradiction with experiments.[2]

While TiO monoxides have long been reported experimentally, ZrO monoxides have not been convincingly observed until recent studies.[13–15] Using electron energy loss spectroscopy (EELS) and atom probe tomography (APT), regions near the metal-oxide interface have been identified with apparent ZrO stoichiometry [see Fig. 5(b) in Ref. 13], but the methods do not allow for crystal structure identification. In the titanium-oxygen system, which has many similarities to the Zr-O system, the rock salt structure, γ-TiO, is observed at high temperatures over a large composition range (for the experimental phase diagram see Ref. 4). At low temperatures, α-TiO, a monoclinic ordering of vacancies on 1/6 of the Ti and O sites, is believed to be the ground state. The rock salt structure in ZrO is listed in crystallographic databases[16,17] and once[18] in recent experimental literature but was not clearly isolated. Additionally, there is a δ-TiO_x phase, observed experimentally[19] with stoichiometry $\sim Ti_3O_2$. In δ-TiO_x, the Ti sublattice has an AlB_2 type structure while oxygen atoms sit in elongated octahedral interstitial positions. The ideal stoichiometry of the structure is TiO, but random vacancies on the oxygen sublattice lead to the observed $\sim Ti_3O_2$ stoichiometry. This rich variety of stable and metastable Ti monoxide structures and Ti-oxides with stoichiometries between $TiO_{1/2}$ and TiO_2 can serve as a guide in the search for a stable Zr monoxide structure.

In this work, we present a systematic investigation of the electronic and thermodynamic properties of the Zr-O system. We performed a large search for ground-state structures throughout the composition range $0 \leqslant x \leqslant 2$ in ZrO_x, with a particular focus on potential compounds of stoichiometry ZrO. We also performed density functional theory (DFT) calculations and fit a cluster expansion for the energetics of octahedral interstitial oxygen incorporation in α-Zr. We considered the electronic structure of the suboxide phases and how it relates to the large oxygen solubility and low volume expansion with increasing oxygen content. Using the cluster expansion formalism and grand canonical Monte Carlo calculations, we constructed a temperature-composition phase diagram at low temperature, predicted the variation of oxygen chemical potential and oxygen partial pressure with oxygen concentration, and analyzed the order/disorder transitions between equilibrium phases.

II. METHODS

A. Candidate structures

Construction of a phase diagram requires a comparison of the free energies of different phases as a function of temperature and composition. Therefore a first step is to identify candidate phases. Since the low-temperature α-Zr phase has an hcp crystal structure and the ZrO_2 structures known experimentally have fcc based Zr lattices (that are potentially distorted as in the tetragonal and monoclinic forms), we initially limited our search for stable ZrO_x phases to crystal structures with hcp and fcc based Zr sublattices. We generated symmetrically distinct candidate structures using the following criteria. For the hcp Zr lattice, we generated the 329 possible ZrO_x structures with oxygen occupying octahedral interstitial positions up to $x = 1$ and up to ten Zr atoms per unit cell. For the fcc Zr lattice, we generated the 2 659 possible ZrO_x structures with oxygen occupying octahedral and tetrahedral interstitial positions up to $x = 2$ and up to eight Zr atoms per unit cell. We also generated the 199 possible structures with O vacancies in the monoclinic α-ZrO_2 structure with up to eight Zr atoms per unit cell. No vacancies were allowed on the Zr lattice in any structures.

To investigate the possibility of a ground-state Zr monoxide, we also performed *ab initio* calculations of structures that have been observed experimentally[4,19] in TiO, replacing Ti with Zr. The calculated phases were based on γ-TiO (rock salt), α-TiO (rock salt with ordered Zr and oxygen vacancies such that 1/6 of the sites are vacant), and hexagonal δ-TiO without the random oxygen vacancies that usually result in the stoichiometry $\sim Ti_3O_2$. δ-TiO consists of ω-Ti with interstitial O. We also considered the structure based on CuTi that was identified as a low energy ZrO structure in previous DFT calculations.[20]

As discussed further in Sec. III A, the DFT calculations with low convergence identified an energetically favorable distortion of δ-ZrO, which we refer to as δ'-ZrO, and a structure with composition Zr_2O_3 as potential ground states. Therefore we also considered the possibility of O vacancy ordering in these structures. For δ'-ZrO, we generated the 260 possible structures with O vacancies not on first nearest-neighbor sites and up to six Zr atoms per unit cell. For Zr_2O_3, we generated the 118 possible structures with O vacancies and up to four Zr atoms per unit cell.

After generating the candidate structures, we performed DFT supercell calculations to determine the total energy of each structure at 0 K. Given a fixed total composition, the ground-state phases at 0 K are those which can not be separated into other phases in a way that lowers the total energy of the system. The set of ground-state structures corresponds to the convex hull in energy-composition space [see Fig. 1(a)].

B. DFT calculations

Ab initio calculations were performed using density functional theory[21] with the Vienna Ab Initio Software Package (VASP) code.[22–26] We used projector augmented wave (PAW) pseudopotentials, and the generalized gradient approximation (GGA) as parameterized by Perdew, Burke, and Ernzerhof (PBE).[27,28] Initially, for computational efficiency, we calculated approximate total energies calculated using a reduced plane-wave energy cutoff of 400 eV and reference pseudopotential valence configuration $5s^1$, $4d^3$ for Zr. Once low-energy structures were identified from the preliminary calculations, accurate total energy calculations were performed using a plane-wave energy cutoff of 600 eV and reference pseudopotential valence configuration $4s^2$, $4p^6$, $5s^1$, $4d^3$ for Zr. In all calculations, we used the standard oxygen pseudopotential with reference valence configuration $2s^2$, $2p^4$, and we used a Γ-point centered Monkhorst-Pack k-point mesh with density in reciprocal space approximately equal to $9 \times 9 \times 9$ in a two-atom hcp primitive cell. Atomic positions, lattice parameters, and angles were allowed to relax for each structure.

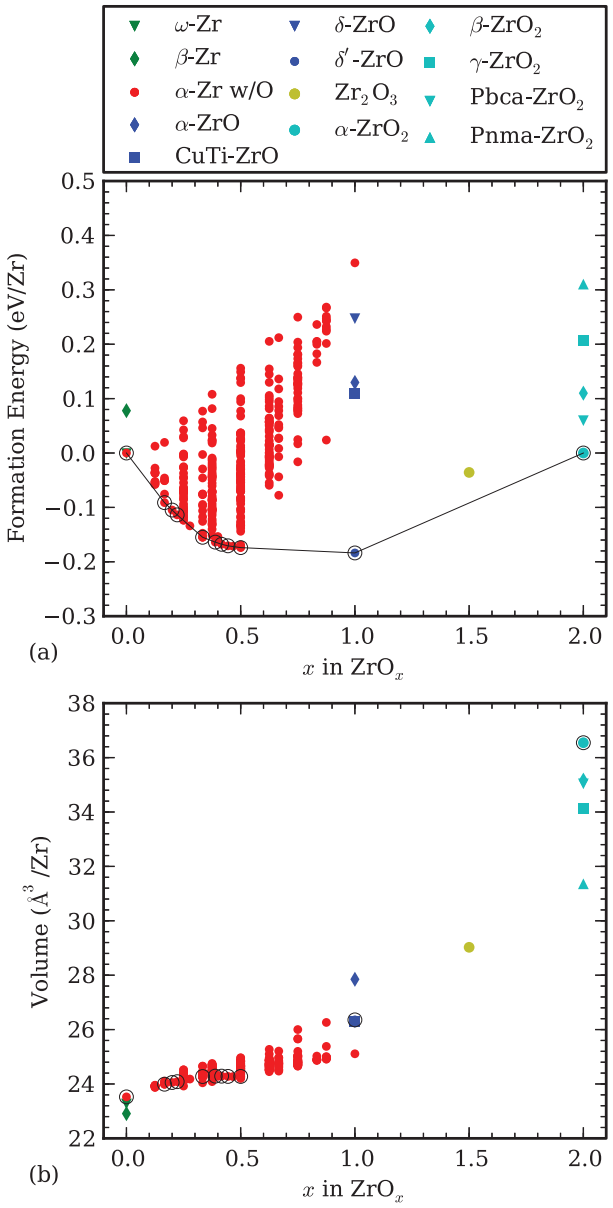

FIG. 1. (Color online) The highly converged calculated (a) formation energy and (b) volume of various crystal structures, using the Zr pseudopotential with reference valence configuration $4s^2, 4p^6, 5s^1, 4d^3$ and energy cutoff 600 eV. The reference structures are α-Zr (without any oxygen) and α-ZrO_2. The structures labeled α-Zr w/O are those generated based on an hcp Zr lattice, but may not be hcp after relaxation. Other notable structures are also indicated. The convex hull is shown with a black line and circles indicating the ground states.

The formation energy normalized per primitive unit cell, e^f, of a particular atomic configuration $\boldsymbol{\sigma}$ with oxygen composition x in ZrO_x, was calculated from DFT total energies (normalized per primitive unit cell) e, using

$$e^f(\boldsymbol{\sigma}) = e(\boldsymbol{\sigma}) - e^{\text{ref}}(x), \tag{1}$$

$$e^{\text{ref}}(x) = e^{\text{ref}}(x_1) + (x - x_1)\frac{e^{\text{ref}}(x_2) - e^{\text{ref}}(x_1)}{x_2 - x_1}, \tag{2}$$

where $e^{\text{ref}}(x_1)$ and $e^{\text{ref}}(x_2)$ are the DFT calculated total energies (normalized per primitive unit cell) of reference states with composition x_1 and x_2, respectively.

C. Depth-first search cluster expansion fitting

The cluster expansion formalism[29,30] is a well established method for constructing an effective Hamiltonian for the configurational energy of a crystal in terms of polynomials of occupation variables describing the atoms occupying the crystal sites. The general form is

$$e^f(\boldsymbol{\sigma}) = V_0 + \sum_\alpha m_\alpha V_\alpha \phi_\alpha(\boldsymbol{\sigma}) \tag{3}$$

in which α indicates an orbit of symmetrically equivalent clusters, m_α is the number of equivalent clusters per primitive unit cell, $\phi_\alpha(\boldsymbol{\sigma})$ is the average value of the polynomial functions for clusters in orbit α, and V_α are expansion coefficients called effective cluster interactions (ECIs) obtained by fitting to *ab initio* energy calculations. Here, we used occupation variables, σ_j, that are 1 if oxygen occupies an interstitial site j and 0 if the site is vacant.

The goal in constructing a cluster Hamiltonian is to determine a limited set of ECIs such that the expansion can be truncated and computational expense is minimized while the predictive power is maximized. In a typical approach, a set of candidate ECI are chosen in some fashion, their values are fit in a least-squares sense to DFT energetics, and the predictive power of the fitted ECI set is judged by calculation of a cross-validation (CV) score. New sets of candidate ECI are chosen, often according to a genetic algorithm,[31] and the optimal set sought by minimizing the CV score.

A genetic algorithm is often quick to find a population of ECI sets with low CV scores, but it is not as efficient at finding an ECI set with a local absolute minimum CV score. A direct minimization procedure that works by testing how small changes to an ECI set affect the CV score and chooses a new ECI set which minimizes the CV score has the problem that it will get trapped in local minima. We found that a simple and effective approach that does not get trapped in local minima is to perform a depth-first search. In this method, a starting ECI set is chosen, fit in a least-squares sense, and the leave one out cross-validation (LOOCV) score is calculated. Being the first step, that LOOCV score is stored as the best-to-date LOOCV score. Subsequently, one by one, each candidate ECI is toggled on or off, the ECI values refit, and LOOCV score calculated. Each of these new ECI sets will differ from the previous ECI set by having one additional ECI either included or excluded. Any new ECI set which lowers the LOOCV score is added to a queue. Next, the ECI set in the queue with the lowest LOOCV score is chosen and the process repeated. The process continues until the chosen ECI set does not beat the best-to-date LOOCV score for N_{stop} consecutive steps. By maintaining a queue of possible results, the depth-first search can back out of local minima and continue the search for the global minimum. Increasing N_{stop} results in a longer, more exhaustive search that can back out of deeper local minima.

We found that it is often very effective to simply perform the depth-first search multiple times, each starting from an initial ECI set with a small number of random interactions

included. While that is the method used in this work, a depth-first search can also be used to perform a final optimization of an ECI set determined by some other method, such as a genetic algorithm[31] or compressive sensing.[32] Compressive sensing can also be an effective way to filter which ECI are allowed candidates prior to performing a depth-first search to find an optimal ECI set.

In order to obtain a better fit for low-energy structures, we determined ECI using weighted least-squares fitting of Eq. (3) by substituting $e^f(\boldsymbol{\sigma})$ with $w(\boldsymbol{\sigma})e^f(\boldsymbol{\sigma})$ and $\phi_\alpha(\boldsymbol{\sigma})$ with $w(\boldsymbol{\sigma})\phi_\alpha(\boldsymbol{\sigma})$. Weights, $w(\boldsymbol{\sigma})$, were determined from the distance, $d(\boldsymbol{\sigma})$, of a structure from the DFT convex hull according to $w(\boldsymbol{\sigma}) = A + B\exp(d(\boldsymbol{\sigma})/k_BT)$, where A is the minimum weight given to structures far from the convex hull, $A + B$ is the maximum weight given to structures on the hull, k_B is the Boltzmann constant, and T is an effective temperature in K that determines the distribution of weights with respect to distance from the convex hull. We used the values $A = 1$, $A + B = 10$, and $k_BT = 0.05$ eV/Zr.

D. Phase diagram construction

Practical approaches for determining phase diagrams using lattice Monte Carlo calculations of thermodynamic properties are well developed.[30,33,34] For each phase under consideration, thermodynamic integration can be used to calculate the Gibbs free energy normalized per primitive unit cell $g(x,T)$ and the grand canonical free energy $\Phi(\mu,T)$, as a function of temperature and composition x, or chemical potential μ, respectively. The stable phase for any value of μ and T is that with the lowest Φ, and first-order phase transition boundaries between a pair of phases U and V are determined by the crossing of grand canonical free energies, i.e., $\Phi^U = \Phi^V$.

Higher-order phase transitions may be characterized by long-range order parameters and divergence of the susceptibility χ or heat capacity C_μ. The susceptibility and heat capacity, which, at constant T and μ, are related to fluctuations in the number of interstitial atoms and grand canonical energy, respectively, are proportional to the second derivative of the grand canonical free energy. These quantities usually diverge at second-order phase transitions as a result of large fluctuations in extensive quantities. Due to the finite size of Monte Carlo simulation cells, though, calculated values of the susceptibility and heat capacity may not exhibit a pronounced divergence, thereby leading to ambiguities in the determination of second order phase boundaries. To this end, it is also useful to simultaneously track long-range order parameters that uniquely characterize ground-state ordered phases.

There are several ways of tracking long-range order in Monte Carlo simulations. One choice is to calculate sublattice concentrations as defined by the supercell of the low-temperature ordered ground state. In the perfectly ordered state, sublattice sites within the supercell characterizing the periodicity of the ordered phase will have different concentrations. This distinction in sublattice concentrations disappears upon crossing an order-disorder phase transition boundary. An order parameter η can therefore be defined as a particular linear combination of sublattice concentrations such that η is 1 for the perfectly ordered state and zero in the fully disordered state.

The existence of several symmetrically equivalent superlattice orderings related to each other by translations of the primitive unit cell can lead to ambiguities when tracking order parameters based on sublattice concentrations. For example, the $ZrO_{1/6}$ ground-state ordering [see Fig. 2(a)], may start with oxygen filling the A site in a given layer, but over the course of the Monte Carlo simulation may collectively drift for many Monte Carlo passes, filling the B site and the C site or shifting along the c axis. Once this occurs, sublattice concentrations are no longer accurate metrics of long-range order.

A more reliable metric of long-range order that is independent of translational shift within Monte Carlo simulations is one evaluated in the reciprocal space of the primitive unit cell. In this work, we tracked simulated diffraction intensities, $I_{\boldsymbol{k}} = S^*_{\boldsymbol{k}}S_{\boldsymbol{k}}$, where $S_{\boldsymbol{k}}$ is the structure factor of the occupation variable,

$$S_{\boldsymbol{k}} = \sum_j \sigma_j \exp(-i\,\boldsymbol{k}\cdot\boldsymbol{r}_j), \tag{4}$$

where $\boldsymbol{r}_j$ is the Cartesian coordinate of crystal site j, $\boldsymbol{k}$ is a reciprocal space vector, and $S^*_{\boldsymbol{k}}$ is the complex conjugate of $S_{\boldsymbol{k}}$. For a supercell, values of $\boldsymbol{k}$ for which $S_{\boldsymbol{k}}$ may be nonzero are integer multiples of the reciprocal supercell lattice vectors. The site coordinate $\boldsymbol{r}_j$ is equal to $\boldsymbol{n}_j + \boldsymbol{\tau}_{b(j)}$, where $\boldsymbol{n}_j$ is the vector to the primitive unit cell containing site j and $\boldsymbol{\tau}_{b(j)}$ is the associated basis vector within the primitive unit cell. This results in a phase difference between the contributions to the $S_{\boldsymbol{k}}$ arising from each basis. These phase differences determine the periodicity of the $S_{\boldsymbol{k}}$ and the range of reciprocal space that should be sampled to find all unique $I_{\boldsymbol{k}}$.

For the hcp Zr crystal structure, we denote the primitive unit cell vectors by $\boldsymbol{a}_1$, $\boldsymbol{a}_2$, $\boldsymbol{c}$ and the reciprocal primitive unit cell vectors as $\boldsymbol{a}^*_1$, $\boldsymbol{a}^*_2$, $\boldsymbol{c}^*$. For our Monte Carlo cells, the supercell lattice vectors are $\boldsymbol{L}_1 = N_1\boldsymbol{a}_1$, $\boldsymbol{L}_2 = N_2\boldsymbol{a}_2$, $\boldsymbol{L}_3 = N_3\boldsymbol{c}$, and the reciprocal vectors of the Monte Carlo supercell are $\boldsymbol{L}^*_1 = \boldsymbol{a}^*_1/N_1$, $\boldsymbol{L}^*_2 = \boldsymbol{a}^*_2/N_2$, $\boldsymbol{L}^*_3 = \boldsymbol{c}^*/N_3$. The basis vectors for the octahedral interstitial sites are $\boldsymbol{\tau}_0 = [0,0,0]$ and $\boldsymbol{\tau}_1 = [0,0,\frac{c}{2}]$. The resulting periodicity of the $S_{\boldsymbol{k}}$ along each reciprocal direction is $\boldsymbol{a}^*_1$, $\boldsymbol{a}^*_2$, and $2\boldsymbol{c}^*$. Throughout this work, we will report $\boldsymbol{k}$ in terms of fractional coordinates of the reciprocal primitive unit cell vectors of the hcp Zr lattice ($\boldsymbol{a}^*_1$, $\boldsymbol{a}^*_2$, $\boldsymbol{c}^*$). To facilitate comparison of $I_{\boldsymbol{k}}$ sampled at different concentrations, we always normalized $I_{\boldsymbol{k}}$ such that $I_{\boldsymbol{k}} = 1$ for $\boldsymbol{k} = [0,0,0]$.

E. Grand canonical Monte Carlo calculations

For free energy integration, grand canonical Monte Carlo calculations were run at increments of 10 K, over the range 10 K $\leqslant T \leqslant$ 1200 K. At each temperature, the oxygen chemical potential μ_O was incremented by 0.01 eV over a large enough range to include the phase boundaries of interest. The calculations were performed in periodic supercells of dimension $10 \times 10 \times 10$ primitive unit cells or larger. For each value of T and μ_O, a GCMC calculation was performed consisting of 1000 equilibrating passes, followed by 2000 passes for calculating the thermodynamic averages. A pass is defined as N_{sites} attempted flips, N_{sites} being the number of sites in the Monte Carlo cell with variable occupation.

Due to numerous nearly degenerate stacking sequences of two-dimensional oxygen ordering parallel to the basal plane

in ZrO_x, the variance in I_k was often much larger than in the concentration or grand canonical energy. Therefore separate GCMC calculations with more passes were necessary to determine higher order phase boundaries. We used a slightly modified version of the methods of Van de Walle and Asta[33] to determine the equilibration time and required averaging time to reach a desired absolute precision of ± 0.02 in $\langle I_k \rangle$, with confidence level 0.99. In some cases, the required precision in $\langle I_k \rangle$ was not reached in 100 000 passes, in which case the calculation was terminated.

III. RESULTS

A. DFT results

1. Ground-state structure search summary

Our preliminary low-convergence DFT calculations (see Supplemental Material[30]) identified seven ground-state structures: α-Zr, $ZrO_{1/6}$, $ZrO_{1/3}$, $ZrO_{1/2}$, δ'-ZrO, Zr_2O_3, and α-ZrO_2. The ground-state structure with composition Zr_2O_3 was the result of a spontaneous relaxation from a α-ZrO_2 based structure. As described further in Sec. III A 6, this structure is fcc-based with O in both tetrahedral and octahedral interstitial positions. This finding is what led us to search a much wider set of fcc-Zr based structures, but no other ground states were identified. The ground-state structure we refer to as δ'-ZrO is described further in Sec. III A 5. It was identified after perturbing perfect δ-ZrO and allowing relaxations. There is no sign from the preliminary low-convergence DFT calculations that δ'-ZrO and Zr_2O_3 exist with significant off-stoichiometry. Therefore for high-convergence DFT calculations only the exact structures δ'-ZrO and Zr_2O_3 were considered.

The formation energies and volumes calculated with fully converged DFT calculations are shown in Fig. 1. Fully converged DFT calculations indicate the structure δ'-ZrO is a ground state, but the structure Zr_2O_3 is not a ground state. The other Zr monoxides we calculated have significantly higher energies than δ'-ZrO, with γ-ZrO (rock salt without any vacancies) having a formation energy of 0.60 eV/Zr, off the scale of Fig. 1(a). As described further in Sec. III A 4, accurate DFT calculations identified several additional α-Zr based ground-state structures besides the major ground states α-Zr, $ZrO_{1/6}$, $ZrO_{1/3}$, and $ZrO_{1/2}$. These additional ground-state structures are ordered stacking sequences that can be enumerated with a "branching" algorithm.[35] While we have only calculated a selection of the infinite possible stacking sequences, these results show that there are likely many (perhaps infinitely many) minor ground-state stacking sequences.

2. ZrO_x major ground-state structures

The structures of the three major ground-state ordered phases in α-Zr predicted by DFT calculations are shown in Fig. 2. All three ground-state ordered phases have $\sqrt{3}a \times \sqrt{3}a$ ordering on the octahedral interstitial sublattice parallel to the basal plane of α-Zr. The $ZrO_{1/6}$ ground-state phase consists of alternating empty and $\frac{1}{3}$-occupied layers of octahedral oxygen in the basal plane. The occupied layers are staggered so that along $\boldsymbol{c}$ there is an $A\_B\_C\_A\_B\_C\_$ ordering of the two-dimensional $\sqrt{3}a \times \sqrt{3}a$ superlattices within the occupied layers, where '_' indicates empty layers and A, B, C, indicate the three translational variants of a $\frac{1}{3}$-occupied layer. The $ZrO_{1/6}$ variant with $A\_B\_A\_B\_$ ordering has an energy within 1 meV/Zr atom of the first variant, which is degenerate within the accuracy of the calculations. The $ZrO_{1/3}$ ground-state phase consists of $\frac{1}{3}$-occupied octahedral oxygen layers staggered with an $ABCABC$ ordering along $\boldsymbol{c}$. The $ZrO_{1/2}$ ground-state phase consists of alternating $\frac{1}{3}$- and $\frac{2}{3}$-occupied octahedral oxygen layers. The occupied positions in the $\frac{1}{3}$-occupied layer are aligned with the vacant positions in the $\frac{2}{3}$-occupied layer. We find that there is very little volume expansion with addition of interstitial oxygen in α-Zr, even for quite unstable structures with oxygen concentration up to ZrO [see Fig. 1(b)]. The lattice expansion along $\boldsymbol{a}$, $\boldsymbol{c}$ and the volumetric expansion is given in Table I for $ZrO_{1/6}$, $ZrO_{1/3}$, $ZrO_{1/2}$ relative to α-Zr.

The $ZrO_{1/3}$ and $ZrO_{1/2}$ predicted ground-state structures are in agreement with the those predicted by Ruban *et al.*,[11] but we also predict the stability of $ZrO_{1/6}$. The cause of the discrepancy can probably be attributed to differences in method. We have calculated the energy of crystal structures with a wide range of compositions directly, while Ruban *et al.* determined the interaction coefficients from dilute concentrations and then used Monte Carlo calculations to predict the stable ground states. Our results for these structures are in agreement with the results of Burton *et al.*[12] and are consistent with neutron diffraction results.[6,36]

Site and orbit-projected density of states (DOS) calculations shown in Fig. 3, predict that the ordered phases are all metallic, as expected. The α-Zr DOS shows a valley at the Fermi level, as is typical for hcp structures.[37] As the oxygen content increases, the oxygen $3s$ states are introduced at $\sim$20 eV below the Fermi level and oxygen $3p$ bonding states are introduced at $\sim$6.7 eV below the Fermi level. While the Zr DOS shows little change below the Fermi level, above the Fermi level increasing oxygen content leads to an increasing density of oxygen $3p$ antibonding states. The high oxygen solubility is related to the fact that the Fermi level stays in the valley typical of hcp structures for oxygen content up to $ZrO_{1/2}$. Since the density of states at the Fermi level remains largely unchanged, so to does the volume of the crystal structure.

3. ZrO_x cluster expansion

We fit a cluster expansion for O-vacancy disorder over the octahedral interstitial sites in α-Zr using the DFT data. We included the 276 configurations with composition $x < 0.7$ and weighted the structures based on their distance from the hull as described in Sec. II C. During the depth-first search ECI optimization procedure we considered clusters with maximum site spacing of 9 Å for pair clusters, 7 Å for triplets, and 6 Å for quadruplets. Then we used the optimized ECI to predict energies for structures with 10 and 12 Zr atoms per unit cell and performed DFT calculations for nine more structures that were predicted to be on or near the convex hull. This identified two new ground-state structures with stoichiometry $ZrO_{1/4}$ and $ZrO_{5/12}$. We then reoptimized our cluster expansion including the nine additional structures.

The final set of optimized ECI consists of a single site term, eight pair interactions, 14 triplet interactions and four

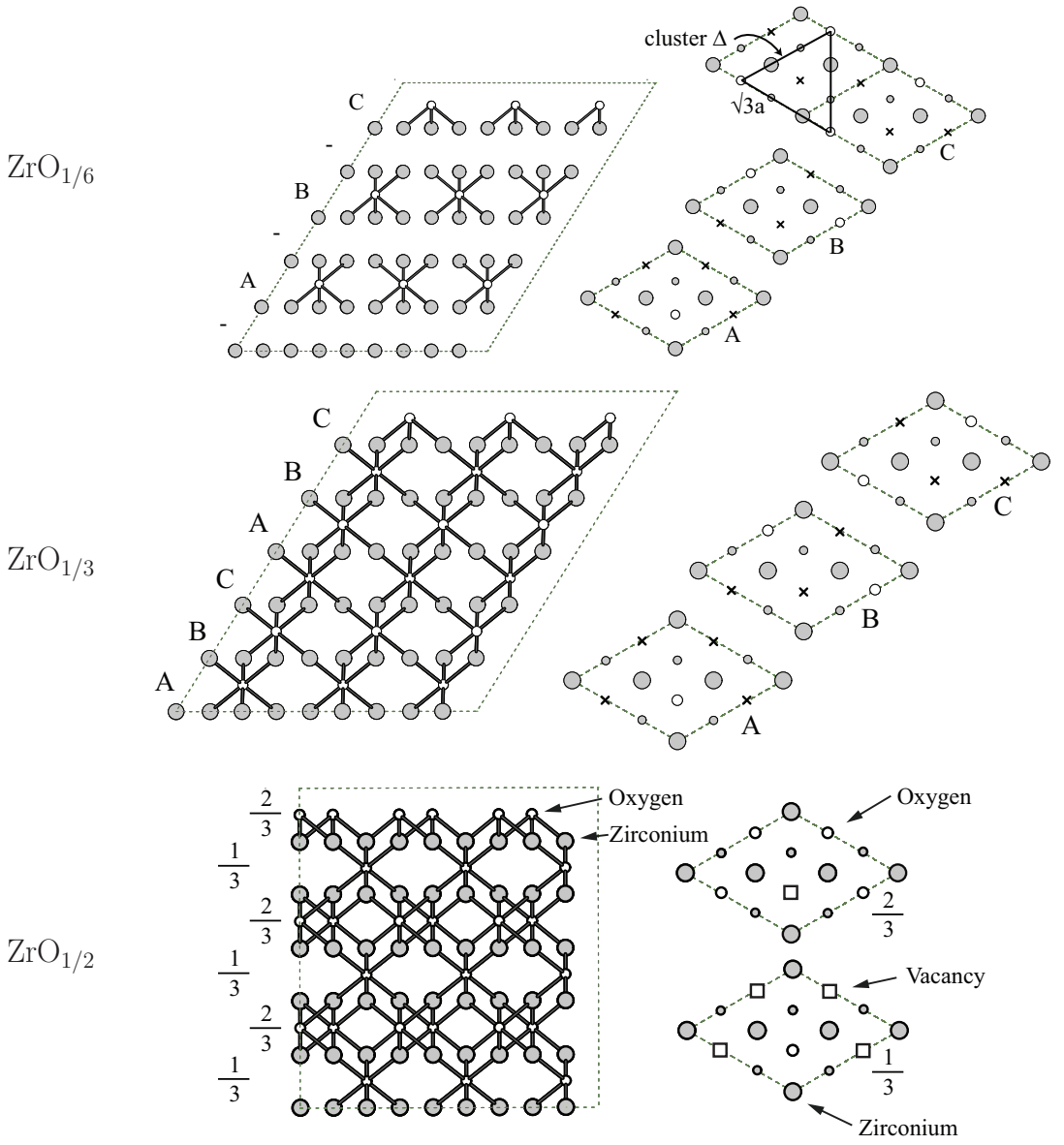

FIG. 2. (Color online) The structure of the major ground-state hcp ordered phases. The gray and white circles indicate Zr and O, respectively. In the plane view, large and small gray circles represent Zr on different [0001] planes and empty squares indicate unoccupied octahedral interstitial sites. The cluster, Δ, corresponding to $\sqrt{3}a \times \sqrt{3}a$ triangle triplets is indicated.

quadruplet terms (see Fig. 4). That the coefficients converge to small numerical values with increasing cluster size justified using a truncated version of the expansion. The root-mean-square error (RMSE) of the cluster expansion fit is 7.8 meV/Zr when including all 285 structures. Due to the weighting, the RMSE is 4.7 meV/Zr for the 133 structures within 100 meV/Zr of the convex hull and 2.7 meV/Zr for the 62 structures within 50 meV/Zr of the convex hull.

TABLE I. Lattice expansion relative to α-Zr.

	a	*c*	Volume
$ZrO_{1/6}$	0.66%	0.65%	1.98%
$ZrO_{1/3}$	1.08%	0.97%	3.17%
$ZrO_{1/2}$	0.84%	1.48%	3.19%

4. ZrO_x stacking sequences

It is clearly preferential for O to avoid nearest-neighbor positions, form $\sqrt{3}a \times \sqrt{3}a$ superlattices within the occupied layers, and for occupied layers on neighboring basal planes to be staggered. There are a large number of possible stacking sequences that follow these rules but which might have long periods with more than 8 Zr atoms per unit cell, the maximum supercell size considered in our original DFT calculations. A "branching" algorithm[35] can be used to enumerate possible stacking sequences. With this approach, in the first generation two generating patterns X and Y, are combined in a superlattice generating a new pattern, XY. In the next generation, the three

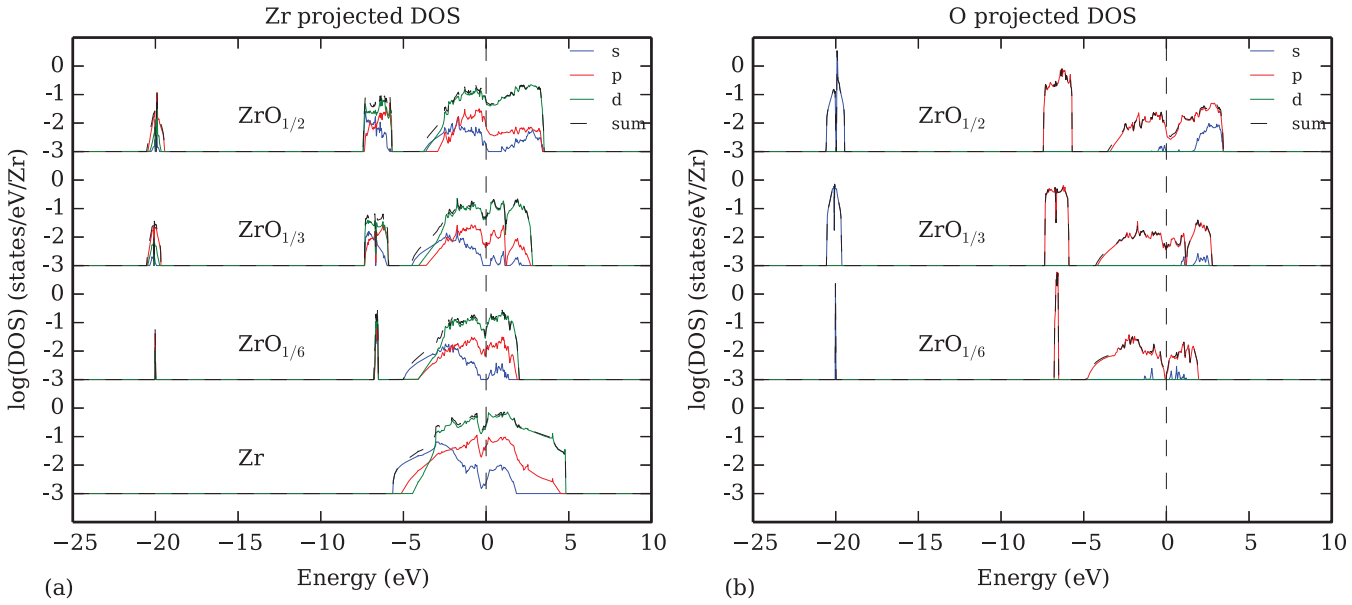

FIG. 3. (Color online) The DOS of the major ground-state hcp ordered phases projected onto (a) Zr and (b) O atomic orbitals, with Fermi level set to 0.

are combined, pairwise, to form the patterns: X, XXY, XY, XYY, and Y. If the patterns are combined again one obtains: X, $XXXY$, XXY, $XXYXY$, XY, $XYXYY$, XYY, $XYYY$, and Y. This process can be repeated *ad infinitum* and then filtered for structures that fit within a given supercell size.

For α-Zr based ordered stacking sequences in the region with composition $0 \leqslant x \leqslant \frac{1}{3}$, the generating structures are an unoccupied layer and a $\frac{1}{3}$-occupied layer. We enforce that $\frac{1}{3}$-occupied layers stack in sequence ABC. These rules result in the following stacking sequences (a '_' again denotes an empty layer): generation 1: _, ABC; generation 2: _, _A_B_C, ABC; generation 3: _, __A__B__C, _A_B_C, _AB_CA_BC, ABC; etc.

In the region with composition $\frac{1}{3} \leqslant x \leqslant \frac{1}{2}$, the generating structures are a $\frac{1}{3}$-occupied layer and a $\frac{2}{3}$-occupied layer. Using similar rules, but not allowing neighboring $\frac{2}{3}$-occupied layers, we obtain the following stacking sequences: generation 1: ABC; generation 2: ABC, $A(BC)$; generation 3: ABC, $AB(AC)BA(BC)$, $A(BC)$; generation 4:

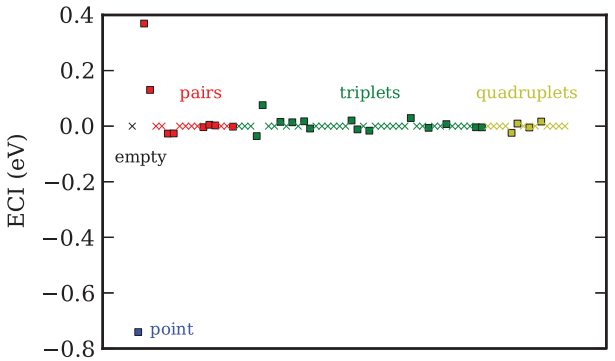

FIG. 4. (Color online) ECI for hcp Zr with octahedral O, with "×" indicating ECI with value 0. Tabulated values of the ECI are included in Ref. 30.

ABC, $ABC(AB)CAB(CA)BCA(BC)$, $AB(AC)BA(BC)$, $AB(CA)B(CA)BC(AB)C(AB)CA(BC)A(BC)$, $A(BC)$; etc. In these, the parentheses indicate a single $\frac{2}{3}$-occupied layer and which two translational variants of the $\frac{1}{3}$-filled layers make up that $\frac{2}{3}$-occupied layer.

The largest cluster included in our cluster expansion is the pair cluster of length $\frac{3}{2}c$ which lies parallel to $\boldsymbol{c}$. This means that the cluster expansion predicted formation energies are identical for stacking sequences that only differ in the fourth-neighbor layer, such as A_B_C_A_B_C_ and A_B_A_B_. Additionally, it means that the cluster expansion predicts the existence of the minor ground states $ZrO_{2/9}$, $ZrO_{1/4}$, and $ZrO_{4/9}$. These have the structures _AB_CA_BC, _ABC, and $AB(CA)BC(AB)CA(BC)$. Stacking sequences which have a larger number of $\frac{1}{3}$-occupied layers between unoccupied or $\frac{2}{3}$-occupied layers lie exactly on the predicted convex hull between these structures and the major ground states. The cluster expansion predicts that there are no minor ground states in the range $0 \leqslant x \leqslant \frac{1}{6}$, because in that region the concentration is too low to force all O to order on the basal plane and it is favorable to decompose into a mixture of disordered α-Zr and ordered $ZrO_{1/6}$.

We performed additional DFT calculations of the minor ground states and several structures predicted by the cluster expansion to lie directly on the convex hull. This resulted in a confirmation of the following structures as DFT predicted ground states: α-Zr, $ZrO_{1/6}$, $ZrO_{1/5}$, $ZrO_{2/9}$, $ZrO_{1/3}$, $ZrO_{7/18}$, $ZrO_{5/12}$, $ZrO_{4/9}$, $ZrO_{1/2}$. The only cluster expansion predicted ground state that was not a DFT predicted ground state is $ZrO_{1/4}$. However, it lies within 1 meV/Zr of the convex hull, so it is within the expected error of the DFT results.

We expect that with enough DFT accuracy many stacking sequences would be identified as ground states. This is consistent with experimental observations[2] of long-period stacking sequences in the range $\frac{1}{6} \leqslant x \leqslant \frac{1}{3}$. We are not aware of experimental observations confirming our prediction of

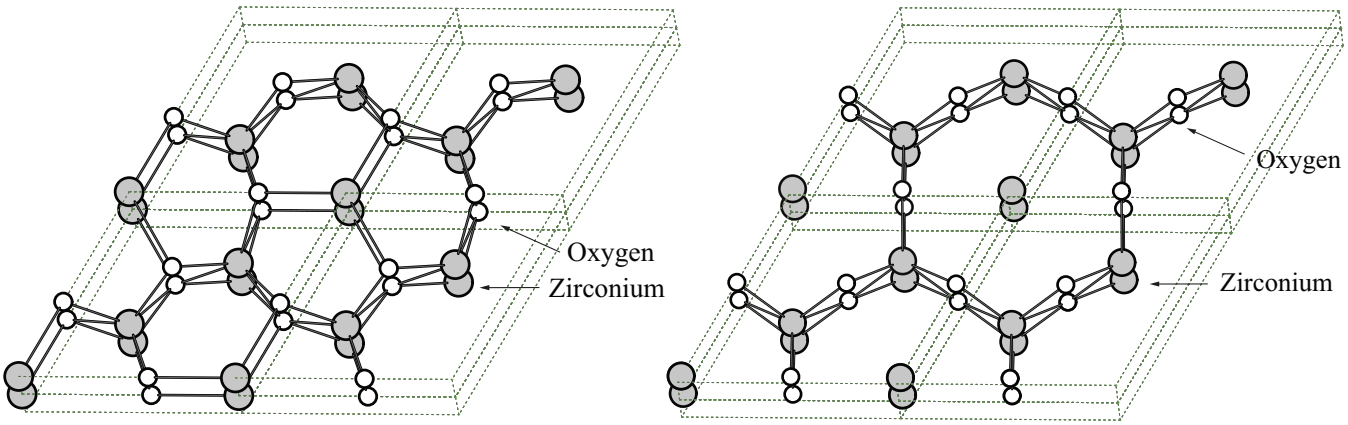

FIG. 5. (Color online) The structure of the (a) ground-state δ'-ZrO phase and (b) mechanically unstable δ-ZrO phase, viewed along the c axis. Gray atoms are Zr and white atoms are O.

long-period stacking sequence ground states in the range $\frac{1}{3} \leqslant x \leqslant \frac{1}{2}$, but the DFT calculations of Burton *et al.*[12] did identify $ZrO_{5/12}$ as a low-temperature ground state. The structures in the range $\frac{1}{3} \leqslant x \leqslant \frac{1}{2}$ are stable for a very small range of μ_O and are expected to be stable only at very low temperatures as seen in in the work of Burton *et al.* for $ZrO_{5/12}$ and in our own GCMC results. This explains why they may not have been observed experimentally and makes our truncation of the interactions at a distance beyond $\frac{3}{2}c$ a good approximation for the temperatures $T > 300$ K of most interest to us. It is beyond the focus of this work to provide a complete accounting of the low-temperature behavior of these stacking sequences beyond noting that it is predicted by the DFT calculations.

5. *ZrO*

Calculations based on the experimentally observed Ti monoxide crystal structures identified the structure shown in Fig. 5(a) and listed in Table II as a 0-K ground state. This structure is significantly more stable than any of the other ZrO structures we calculated. We refer to the ground-state structure as δ'-ZrO since its structure is based on the δ-TiO crystal structure, shown in Fig. 5(b) for δ-ZrO. In δ'-ZrO Jahn-Teller oxygen distortions lower the total energy of the structure by 446 meV/Zr. Figure 6 shows the effect of the Jahn-Teller distortion to reduce the DOS at the Fermi level. There are two symmetrically equivalent distortions that can occur, so that δ-ZrO exists as a mechanically unstable saddle point between two equivalent δ'-ZrO structures, as confirmed by nudged elastic band (NEB) calculations.[30] Upon distorting, the O become fivefold coordinated with Zr forming a polar pyramid with square base. The four Zr comprising the square base are located on the 2d Wyckoff sites, and the one Zr comprising the peak of the pyramid is located on a 1a Wyckoff site. In the δ'-ZrO structure, any three oxygen which share a Zr neighbor all have their polar axis pointing in different directions. This likely results in strong interactions between the distortions of nearby oxygen, and leads to the stability of this particular structure. Some of the energy lowering is probably also due to the change in the density of states around

TABLE II. Structure of the calculated hexagonal δ'-ZrO ground-state phase.

	Phase:	δ'-ZrO
	Space group:	$P\bar{6}2m$
	Lattice parameters:	$a = 5.285$ Å
		$c = 3.179$ Å
Atom	Wyckoff site	Position
Zr	1a	(0, 0, 0)
Zr	2d	(1/3, 2/3, 1/2)
O	3f	(0.407, 0, 0)

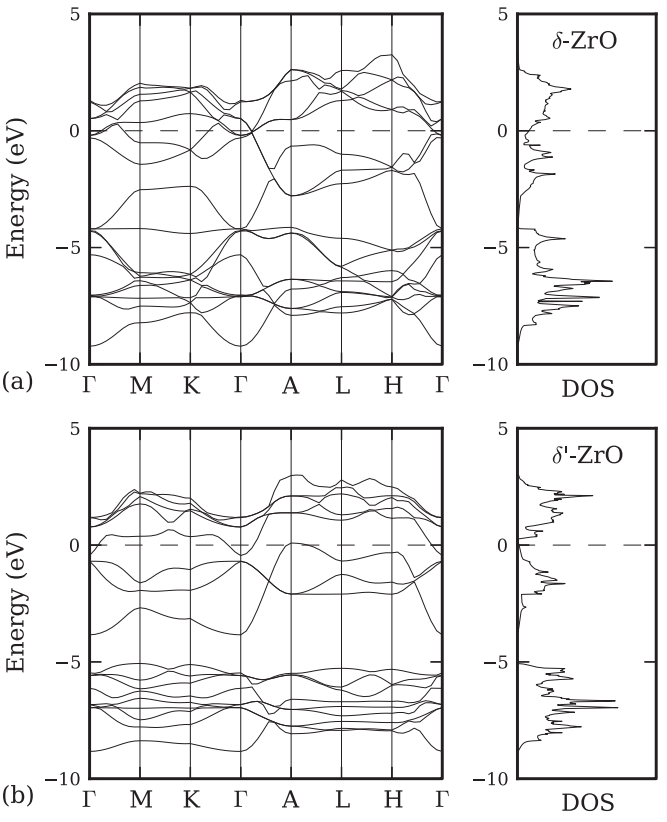

FIG. 6. The band structure and DOS of the (a) mechanically unstable δ-ZrO phase and (b) ground-state δ'-ZrO phase, with Fermi level set to 0.

TABLE III. Structure of the calculated tetragonal Zr_2O_3 metastable phase.

	Phase:	Zr_2O_3
	Space group:	$P\bar{4}m2$
	Lattice parameters:	$a = 3.129$ Å
		$c = 5.737$ Å
Atom	Wyckoff site	Position
Zr	2g	(0, 1/2, −0.249)
O	2g	(0, 1/2, 0.362)
O	1a	(0, 0, 0)

the Fermi level. As shown in Fig. 6, the distortion pushes down occupied electronic states close to the Fermi level while lifting unoccupied electronic states without any energy penalty. We also calculated the energy of a structure in which the oxygen distorted in opposite directions on alternating basal plane layers. This staggered structure was 200 meV/Zr higher energy than the ground state.

6. Zr_2O_3

Our preliminary low-convergence DFT calculations identified a tetragonal phase with stoichiometry Zr_2O_3 as being a potential ground state, but high-convergence DFT calculations indicate that Zr_2O_3 is actually a metastable phase 56 meV/Zr above the convex hull. This phase has also been recently investigated by Xue *et al.*[38] in the Hf-O and Zr-O systems using DFT calculations. The structure is tetragonal with space group $P\bar{4}m2$, as detailed in Table III. Oxygen interstitials exist in two layers perpendicular to the tetragonal c axis. The first layer, consisting of one third of the total oxygen atoms, contains oxygen in half of the tetrahedral interstitial positions. The second layer consists of the remaining two thirds of the oxygen atoms, located in octahedral interstitial positions. The octahedral oxygen are shifted out of the ideal octahedral positions due to repulsion from the tetrahedral oxygen. Since the tetrahedral oxygen atoms only occupy one half of the possible tetrahedral interstitial sites, it is possible for them to occupy one half in one tetrahedral layer, and the other half in other tetrahedral layers. The structure, which has $ABAB$-type stacking of the tetrahedral layers, has an energy only 8 meV/Zr higher than the minimum energy Zr_2O_3 structure in which the same half of the tetrahedral sites is occupied in every layer.

The work of Xue *et al.* showed that $(Hf,Zr)_2O_3$ is stable relative to metallic (Hf,Zr) and O_2 and proposed that the Hf_2O_3 phase might explain the existence of a low-resistance state in hafnia-based resistive random access memory. We have not calculated energies for the Hf-O system, but we predict that in equilibrium Zr_2O_3 would decompose into δ'-ZrO and α-ZrO_2.

B. Predicted phase diagram

We constructed the phase diagram shown in Fig. 7 based on the results of the grand canonical Monte Carlo calculations in the concentration range $0 \leqslant x \leqslant 0.5$. Note that the composition axis of the calculated phase diagram is in terms of atomic fractions (i.e., y in $Zr_{1-y}O_y$) as opposed to the fraction of filled interstitial sites (i.e., x in ZrO_x). This facilitates comparison with binary phase diagrams of this system in the literature. As this section describes in detail, we identified two-phase boundaries using free energy integration and we identified higher-order transitions by following the simulated diffraction intensities. We included δ'-ZrO in the phase diagram as a line compound since our low-convergence DFT calculations do not indicate a capacity for significant off-stoichiometry.

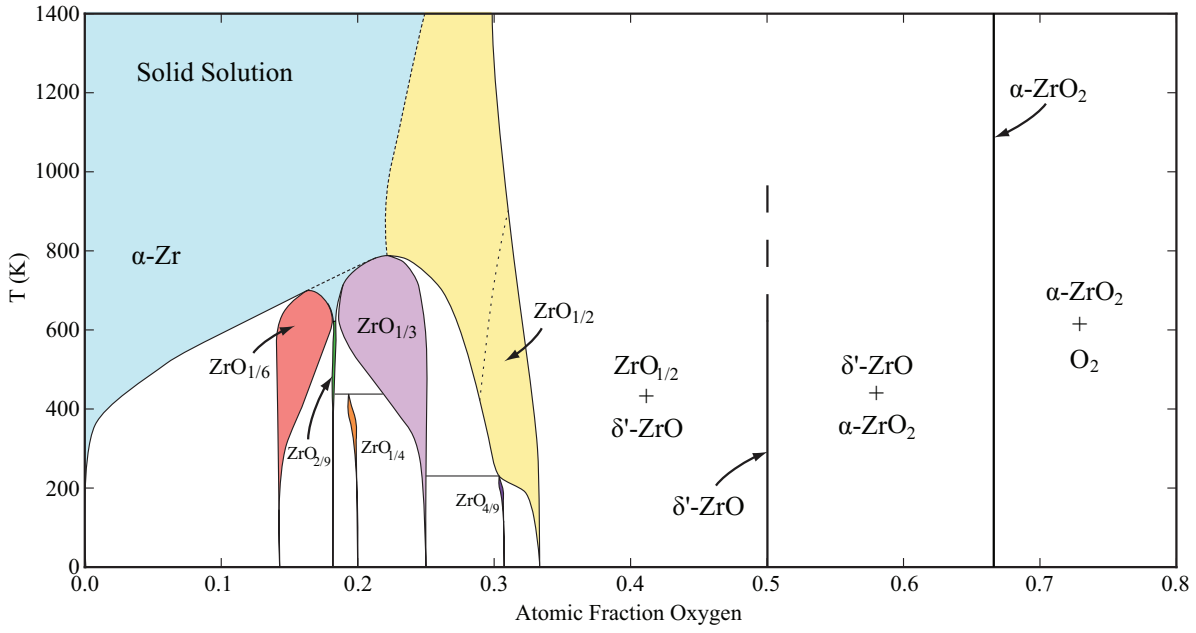

FIG. 7. (Color online) The calculated phase diagram of hcp ZrO_x. Colored areas indicate single phase regions, and uncolored areas indicate two-phase regions. Solid lines indicate first-order phase boundaries, and dashed lines indicate higher-order transitions. The region between $ZrO_{1/6}$ and $ZrO_{1/3}$ is shaded the same color as solid solution α-Zr since it has no long-range order parallel to $\boldsymbol{c}$.

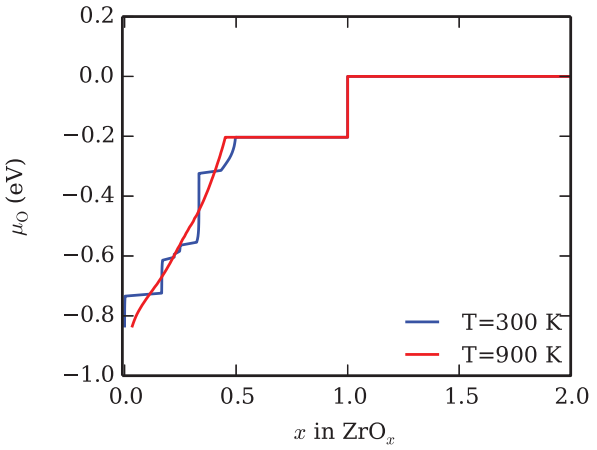

FIG. 8. (Color online) Oxygen chemical potential for the Zr-O system. μ_O is referenced to the two-phase region with Zr_2O_3 and α-ZrO_2. Regions with increasing μ_O correspond to single phase regions, while μ_O remains constant in two-phase regions.

1. Two-phase boundaries

From GCMC calculations, we obtained results for oxygen content x as a function of μ_O and T. We started GCMC calculations in each of the cluster expansion ground states and approached each two-phase regions from the direction of both increasing and decreasing μ_O. We used free energy integration to obtain the free energy as a function of μ_O and T. The equilibrium phase is the one which has the minimum free energy at a given μ_O and T. Figure 8 shows μ_O as a function of x for the equilibrium phase. Given a particular temperature, regions in Fig. 8 in which μ_O is constant with increasing x correspond to two-phase regions in the phase diagram. Regions in which μ_O increases with increasing x correspond to single phase regions in the phase diagram. Sharp increases in μ_O correspond to line compounds or single phase regions with limited range in composition.

2. Disordering of $ZrO_{1/2}$

The simulated diffraction intensities clearly indicate two disordering transitions occur in $ZrO_{1/2}$ with either increasing temperature or decreasing x. Perfectly ordered $ZrO_{1/2}$, which has alternating $\frac{1}{3}$-occupied and $\frac{2}{3}$-occupied layers, has three diffraction spots: one with $I_{\boldsymbol{k}_A} = \frac{1}{9}$ at $\boldsymbol{k}_A = [0,0,1]$, and two with $I_{\boldsymbol{k}_B} = \frac{4}{9}$ at $\boldsymbol{k}_{B_1} = [\frac{1}{3},\frac{1}{3},1]$ and $\boldsymbol{k}_{B_2} = [\frac{2}{3},\frac{2}{3},1]$. Figure 9 shows the value of $I_{\boldsymbol{k}}$ as obtained from GCMC calculations starting at $x = \frac{1}{2}$ and decreasing x (decreasing μ_O) over the temperature range 200 K $\leqslant T \leqslant$ 2500 K. The low-temperature disordering transition finishes at $T \approx 1500$ K and is associated with the disappearance of $I_{\boldsymbol{k}_A}$. The high-temperature disordering transition finishes at $T \approx 2150$ K and is associated with the disappearance of $I_{\boldsymbol{k}_B}$.

Our simulated diffraction results are in agreement with neutron diffraction experiments,[36] though the experimentally observed transitions occur at $T \approx 770$ and $\approx$1310 K. The difference in transition temperature is possibly due to uncertainty in the experimental concentration, which is likely less than $x = \frac{1}{2}$ due to oxygen loss at high T. The disappearance of $I_{\boldsymbol{k}_A}$ and then $I_{\boldsymbol{k}_B}$ was attributed to "the rearrangement

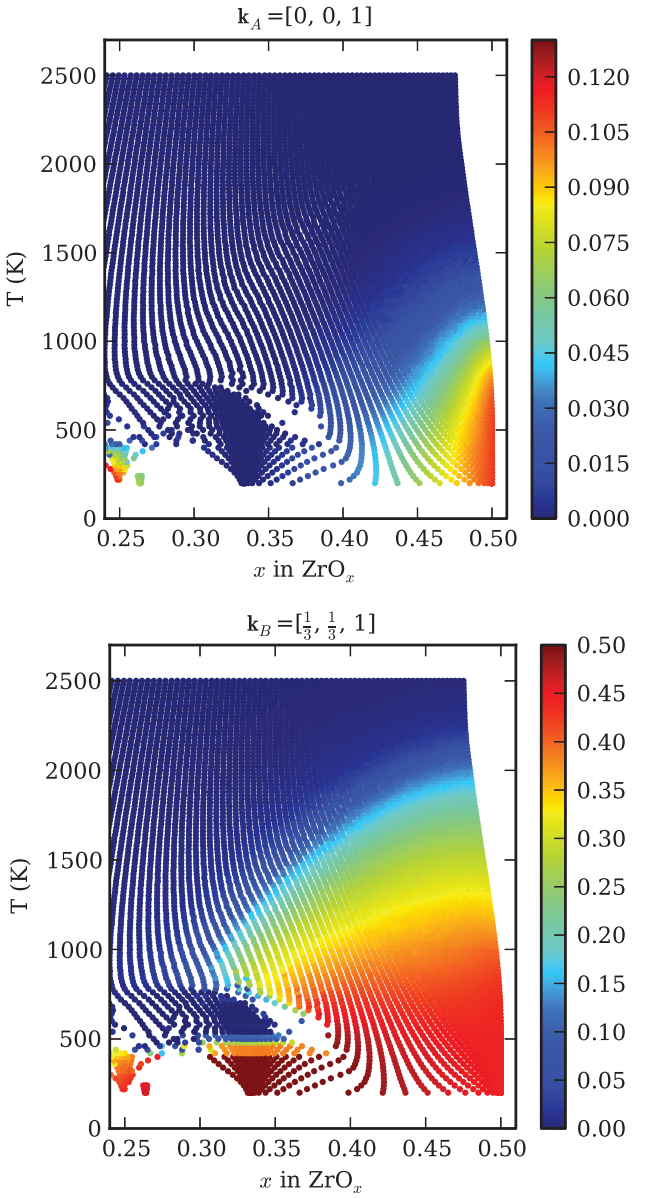

FIG. 9. (Color online) The values of the simulated diffraction intensities $I_{\boldsymbol{k}}$ for (a) $\boldsymbol{k}_A = [0,0,1]$ and (b) $\boldsymbol{k}_B = [\frac{1}{3},\frac{1}{3},1]$, obtained from GCMC calculations with decreasing μ_O (decreasing x), over the range 200 K $\leqslant T \leqslant$ 2500 K.

of the oxygen atoms from uneven to even distribution on the neighboring interstice planes, and then [to a] random distribution in each plane."[36] This conflicts with the results of Ref. 12, which identified the low-temperature transition as first-order and the high-temperature disordering as second-order. That work found that the average structure above the first transition temperature maintained alternating O-rich and O-poor layers before fully disordering after the high-temperature transition.

We performed a detailed analysis[30] of the disordering process for a series of GCMC calculations performed with μ_O corresponding to the highest concentrations in Fig. 9 and T increasing from 200 to 2500 K. The results in Fig. 10(a) show $I_{\boldsymbol{k}_A}$ vanishing over the range 700 K $\leqslant T \leqslant$ 1500 K and $I_{\boldsymbol{k}_B}$ vanishing at $T \approx 2150$ K. In Fig. 10(b), we observe a

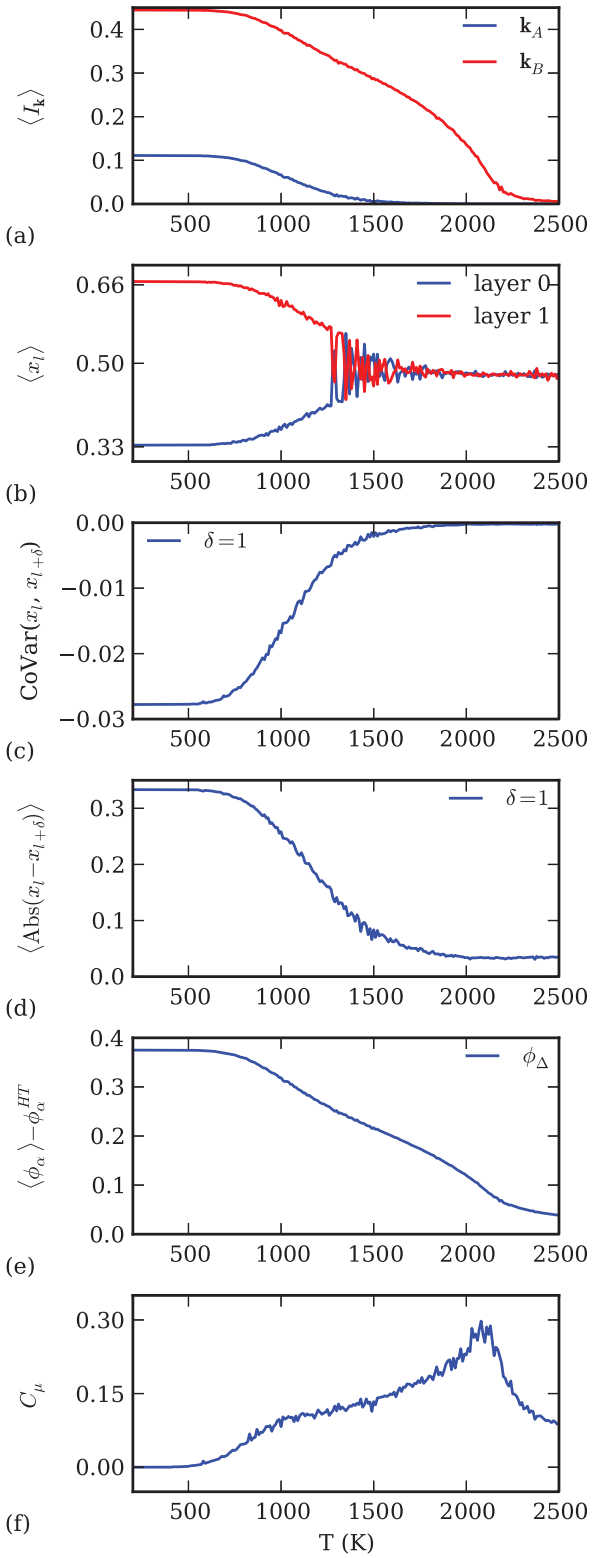

FIG. 10. (Color online) Analysis of the $ZrO_{1/2}$ disordering process with increasing temperature, obtained from a series of GCMC calculations with μ_O corresponding to the maximum concentration in Fig. 9 and increasing T in $12 \times 12 \times 12$ supercells. x_l is the O concentration in basal layer l of the simulation cell.

distinction between O-rich and O-poor supercell layers up to $T \approx 1300$ K, significant scatter over the range 1300 K $\leqslant T \leqslant 1700$ K, and finally no distinction between O-rich and O-poor supercell layers above $T \approx 1700$ K. This indicates that above $T \approx 1300$ K the GCMC calculations begin sampling the symmetrically equivalent configurations of $ZrO_{1/2}$ which are obtained by a translation of $\frac{1}{2}\boldsymbol{c}$ from the initial configuration, and demonstrates that it is necessary to use order parameters that are invariant with respect to translation.

By comparing Fig. 10(a) with Figs. 10(c) and 10(d), we observe that the covariance and mean absolute difference in the O concentration on neighboring basal layers decrease to zero and a small number, respectively, over the same temperature range that $I_{\boldsymbol{k}_A}$ vanishes. This indicates that above the first disordering temperature upon heating the correlation between O-rich and O-poor neighboring layers vanishes and the only differences in O concentration are the small differences due to random fluctuations. Long-range order remains up to the second disordering transition when $I_{\boldsymbol{k}_B}$ vanishes. The long-range order largely depends on the $\sqrt{3}a \times \sqrt{3}a$ ordering parallel to the basal plane. We analyzed the temperature dependence of this short-range ordering in Fig. 10(e) using the difference $\langle \phi_\alpha \rangle - \phi_\alpha^{HT}$, where the correlations in the high temperature limit are $\phi_\alpha^{HT} = \langle x \rangle^m$, m being the number of sites in cluster α. Comparing Figs. 10(a) and 10(e) shows a direct correlation between long-range disordering and the reduction in the short-range correlations of the cluster that corresponds to $\sqrt{3}a \times \sqrt{3}a$ triangle triplets in the basal plane (see Fig. 2). Figure 10(f) shows that only the high-temperature disordering, which results in a loss of long-range order, is associated with a divergence in the heat capacity C_μ.

We performed a similar analysis of the disordering process for a series of GCMC calculations performed at 1000 K and O concentration decreasing to $x = 0.2$. The results, shown in Fig. 11, demonstrate that the disordering process with decreasing O concentration is similar to the disordering with increasing temperature. At $T = 1000$ K, the correlation between O-rich and O-poor neighboring layers vanishes around $x \approx 0.37$ and long-range ordering vanishes at $x \approx 0.30$, which corresponds to a significant increase in the susceptibility, χ_O.

The locations of the low-temperature and high-temperature disordering transitions shown in the phase diagram (see Fig. 7) correspond to the values of x and T at which $I_{\boldsymbol{k}_A} = 0.03$ and $I_{\boldsymbol{k}_B} = 0.05$. Since short-range order and the finite size of the supercells prevent simulated diffraction peaks from being identically zero at the transition temperature, the value $I_{\boldsymbol{k}_B} = 0.05$ was chosen to correspond most closely to the observed peaks in C_μ and χ_O. The disordering transition associated with $I_{\boldsymbol{k}_A}$ shows no divergence in the heat capacity or susceptibility, and the value $I_{\boldsymbol{k}_A} = 0.03$ was simply chosen to indicate a composition-temperature line at which most of the correlation between O-rich and O-poor layers has vanished.

Our results, showing that the low-temperature disordering transition is associated with the vanishing difference between neighboring O-rich and O-poor layers, are clearly in agreement with the analysis of the neutron diffraction experiments.[36] The identification of this loss of order along $\boldsymbol{c}$ as a gradual process rather than as a first-order phase transition was made possible with the use of translationally invariant simulated diffraction intensities as a long-range order parameter.

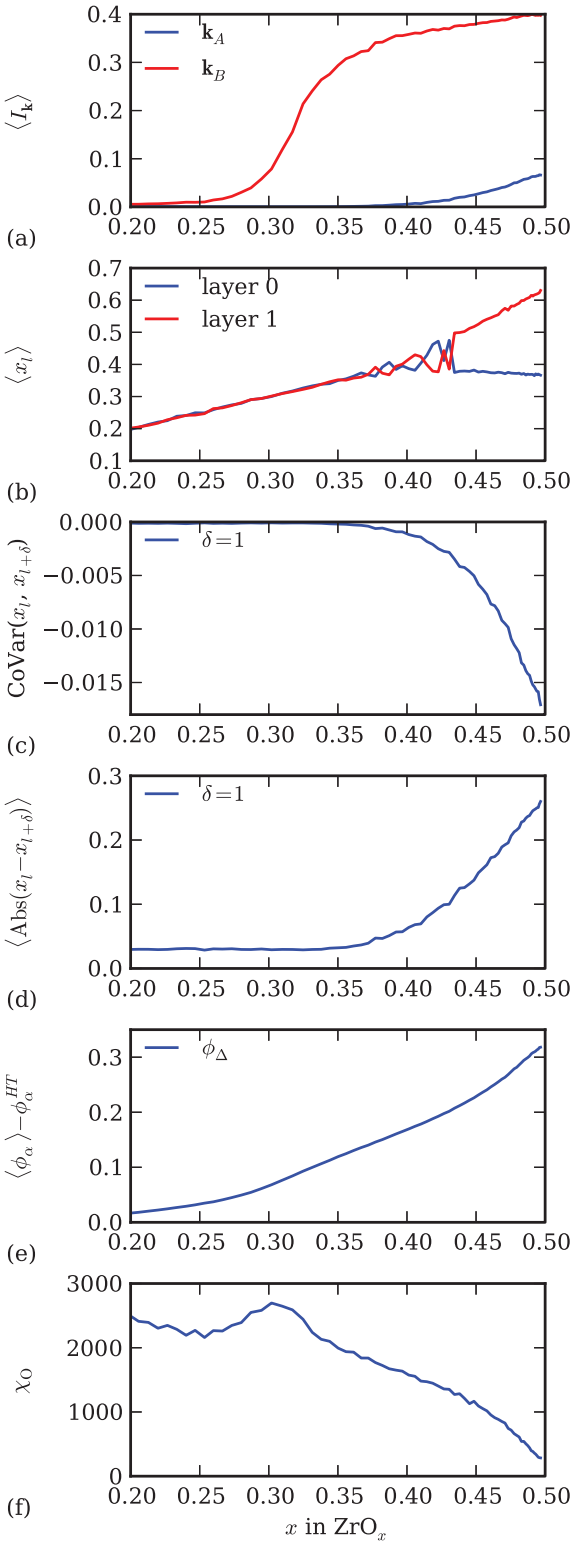

FIG. 11. (Color online) Analysis of the $ZrO_{1/2}$ disordering process with decreasing x at constant $T = 1000$ K, obtained from a series of GCMC calculations in $12 \times 12 \times 12$ supercells. x_l is the O concentration in basal layer l of the simulation cell.

3. *Maximum O solubility in α-Zr*

The experimental phase diagram,[2] indicates a low-temperature solubility of up to 28.6 at% O in α-Zr. The DFT calculations predict $ZrO_{1/2}$ as a ground-state structure, which corresponds to 33 at%. A possible explanation for the discrepancy that is consistent with the GCMC calculations is that the solubility is lower at high temperatures and complete incorporation of 33 at% O is kinetically limited so that it is not observed in practice. In the phase diagram, we draw the maximum O solubility using the values of x and T calculated using μ_O equivalent to the 0-K equilibrium between $ZrO_{1/2}$ and ZrO.

4. *$ZrO_{1/6}$ and $ZrO_{1/3}$*

Accurate GCMC calculations in the region between $ZrO_{1/6}$ and $ZrO_{1/3}$ are challenging due to the large number of nearly degenerate stacking sequences and their sensitivity to supercell size. We found that the required convergence in composition and grand canonical energy were achieved within a few 1000 passes, but that often greater than 10^5 or 10^6 passes were required for convergence of $I_{\boldsymbol{k}}$. A careful examination (see Supplemental Material[30]) of the atomic configurations in this region shows that it is characterized by the arrangement of O atoms into nominally vacant and $\frac{1}{3}$-occupied layers with long-range $\sqrt{3}a \times \sqrt{3}a$ ordering within the basal plane, but that perpendicular to the basal plane there is only short-range order. A convergence study beyond the scope of this work is needed to determine whether this region would persist in the limit of large supercells.

IV. DISCUSSION

A key result of this study is the calculated temperature-composition phase diagram of the Zr-O system shown in Fig. 7. The phase diagram was constructed from first principles using DFT-PBE to calculate the energies of a large number of candidate structures in the Zr-O system and a statistical mechanical treatment relying on a cluster expansion and Monte Carlo simulations to calculate finite temperature free energies.

The phase diagram shows that three classes of oxides are stable in the Zr-O system. The first is the well-known monoclinic ZrO_2, which is predicted to be stable as a line compound. At higher temperature, ZrO_2 transforms to tetragonal ZrO_2 and then to cubic ZrO_2. These oxides are all insulators and highly ionic.

A second class of oxides in the Zr-O system comprises the rich variety of ZrO_x suboxides obtained by dissolving oxygen into hcp Zr. The calculated phase diagram shows that oxygen can dissolve into ZrO_x up to $x \approx \frac{1}{2}$. At high temperature, oxygen dissolves as a solid solution in which interstitial oxygen and vacancies lack any long-range order. At low temperature, though, the oxygen and vacancies are predicted to order, always forming a $\sqrt{3}a \times \sqrt{3}a$ superlattice periodicity perpendicular to the c-axis of the hcp Zr host crystal. Our first-principles DFT-PBE calculations confirm that a large number of suboxides having stoichiometries between $x = \frac{1}{6}$ and $\frac{1}{2}$ are stable at zero Kelvin. Only a subset of these ordered phases continue to be stable at elevated temperature, though, with ordering at $x = \frac{1}{6}$, $\frac{1}{3}$, and $\frac{1}{2}$ persisting to 600 K and beyond.

Similar suboxides as those in Zr-O are seen in the Ti-O[42] and Hf-O[43] systems. The DFT calculated $TiO_{1/6}$, $ZrO_{1/6}$,

and $HfO_{1/6}$ ground-state structures are similar, consisting of alternating empty and staggered $\frac{1}{3}$-filled octahedral oxygen interstitial layers. The DFT calculated ground-state $TiO_{1/3}$ structure differs from the $ZrO_{1/3}$, and $HfO_{1/3}$ structures, consisting of alternating empty and $\frac{2}{3}$-filled layers while the $ZrO_{1/3}$ and $HfO_{1/3}$ structures consist of staggered $\frac{1}{3}$-filled layers. In $ZrO_{1/3}$, the calculated ground state has ABC stacking, while in $HfO_{1/3}$ it has ABAC stacking, though the energy differences between these variants are very small. The DFT calculated $ZrO_{1/2}$ and $HfO_{1/2}$ ground-state structures are identical, with (AB)C type stacking of alternating 2/3-filled and 1/3-filled layers. DFT calculations[42] indicate that the $TiO_{1/2}$ ground-state structure is different; it does not have $\sqrt{3}a \times \sqrt{3}a$ ordering in the basal plane, and instead, has $\frac{1}{2}$-filled layers, with AB stacking such that first nearest-neighbors along the c axis are not occupied. The DFT calculated $TiO_{1/2}$ ground-state structure was found to be significantly more stable than the experimentally reported structure.[42] With that exception, all of these calculated ground-state structures are in good agreement with experimental diffraction observations of the suboxide phases.[5,6,12,42,43]

The $ZrO_{1/6}$ phase transforms to the solid solution α-ZrO_x upon heating or upon decreasing of the oxygen concentration through a first-order phase transition. Ordered $ZrO_{1/6}$ is separated from the α-ZrO_x solid solution by a large two-phase region. The ordered $ZrO_{1/2}$ phase, having layers with an oxygen concentration of $\frac{1}{3}$ alternated by layers with a $\frac{2}{3}$ concentration, maintains its long-range order to very high temperatures. Nevertheless, it undergoes a gradual reduction of ordering over a wide temperature and composition range before completely losing any semblance of long-range order. The phase diagram shows two dashed lines separating $ZrO_{1/2}$ from the solid solution. The outer dashed line denotes a true thermodynamic transition corresponding to a second-order phase transformation. The inner dashed line in an approximate way demarcates a gradual transition in which the distinction in oxygen concentration between adjacent layers perpendicular to the c axis of hcp Zr gradually disappears. This gradual transition is not accompanied by a divergence in either the heat capacity or susceptibility and therefore cannot rigorously be characterized as a thermodynamic transition. Nevertheless, it does coincide with a pronounced change in order parameters, albeit over an extended temperature and composition range.

The ordered $ZrO_{1/3}$ phase is also stable to reasonably high temperatures and over a wide oxygen concentration interval. A two-phase region separates $ZrO_{1/3}$ from the $ZrO_{1/2}$ phase. Several other suboxide phases are predicted to be stable between $ZrO_{1/6}$ and $ZrO_{1/3}$, but are only stable at low temperature and in narrow concentration ranges. At intermediate temperature around 600 K, there is an intermediate phase that separates $ZrO_{1/6}$ and $ZrO_{1/3}$. This phase is similar to $ZrO_{1/6}$ and $ZrO_{1/3}$ with $\sqrt{3}a \times \sqrt{3}a$ ordering in the basal plane. However, instead of exhibiting long-range order along the c axis, this intermediate phase is characterized by strong short-range order with filled oxygen layers having a $\frac{1}{3}$ oxygen occupancy preferentially adjacent to empty layers. A convergence study beyond the scope of this work is needed to determine whether this intermediate phase would persist in the large-size limit.

Finally, we also predict the stability of a third class of oxide in the Zr-O system, having monoxide stoichiometry, which based on 0-K DFT calculations also exists as a line compound. To our knowledge, this is the first prediction of a thermodynamically stable Zr monoxide phase relative to two-phase decomposition into ZrO_2 and $ZrO_{1/2}$. The monoxide, here labeled δ'-ZrO due to its crystallographic similarity to δ-TiO, consists of a Zr sublattice identical to the Zr ω phase with oxygen occupying interstitial sites within that framework. Unlike the ZrO_2 phases, δ'-ZrO is predicted with DFT-PBE to be metallic with a finite density of states at the Fermi level. We did not analyze the stability of δ'-ZrO relative to ZrO_2 and the suboxide $ZrO_{1/2}$ at finite temperature (i.e., by considering vibrational free energies) and are therefore uncertain as to the temperature at which δ'-ZrO may no longer be stable. We denote this uncertainty in the phase diagram with a dashed line for ZrO at higher temperature.

Our calculated phase diagram is consistent with the experimentally observed microstructure if we include the ZrO phase that has been observed recently.[13–15] While the phase diagram indicates wide two-phase composition regions for $ZrO_{1/2}$ with δ'-ZrO and δ'-ZrO with α-ZrO_2, these correspond to very small ranges in oxygen partial pressure (see Supplemental Material[30,39,40]). This makes it unsurprising that δ'-ZrO has not been widely observed previously, since at typical oxidation conditions it is only predicted to be stable in a very small region at the metal-oxide interface, and its nucleation may be limited by interfacial energy, strain energy, and kinetics. Preliminary DFT calculations[41] have shown that this structure is also the ground state in stoichiometric TiO, and it is deserving of attention in HfO as well.

The high oxygen solubility in hcp Zr is quite unique among metals (with the exception of Ti and Hf) and seems to have an electronic origin. As the calculated electronic densities of states for $ZrO_{1/6}$, $ZrO_{1/3}$ and $ZrO_{1/2}$ show (see Fig. 3), the addition of oxygen does not qualitatively modify the electronic densities of states at the Fermi level. While new electronic states appear at energies well below the Fermi level, the characteristic valley at the Fermi level, responsible for the stability of the hcp crystal structure for Ti, Zr, and Hf,[37] remains essentially unchanged with the introduction of oxygen. The lack of any qualitative change in the electronic structure around the Fermi level is likely also responsible for a negligible change in the volume of hcp Zr as a function of oxygen concentration.

Our finite temperature analysis of phase stability has revealed a complex sequence of order-disorder phenomena of the interstitial oxygen over the octahedral sites of hcp Zr. All suboxide ground states within hcp based ZrO_x have the same $\sqrt{3}a \times \sqrt{3}a$ periodicity parallel to the basal plane of the hcp crystal structure. Differences between ground states arise from variations in the oxygen concentration within layers parallel to the basal plane as well as variations in stacking sequences along the c axis of the hcp crystal. As the coefficients of the cluster expansion clearly demonstrate, nearest neighbor oxygen-oxygen interactions, both parallel and perpendicular to the basal plane, are strongly repulsive. Oxygen therefore strives to surround itself by as many vacancies as possible within its nearest neighbor shell. This results in the

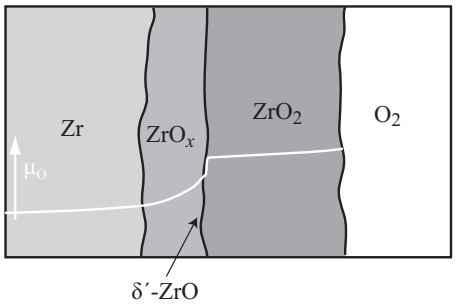

FIG. 12. Schematic of the microstructure observed experimentally during Zr oxidation, along with the variation of μ_O with distance from the surface.

characteristic $\sqrt{3}a \times \sqrt{3}a$ super lattice periodicity common to all the suboxide ground states. The allowed in plane concentrations consistent with $\sqrt{3}a \times \sqrt{3}a$ periodicity are $x = \frac{1}{3}$ and $\frac{2}{3}$ and different stackings of empty, $\frac{1}{3}$-filled and $\frac{2}{3}$-filled layers result in a hierarchy of ordered phases having different concentrations and having energies that reside on the convex hull. The finite temperature Monte Carlo simulations show that the in-plane oxygen ordering is very stable, persisting to high temperature, while interactions that determine relative stacking sequences of in-plane orderings are weaker, leading to the onset of disorder along the c axis at lower temperature.

The solubility and ordering properties of oxygen in hcp Zr are very similar to those of intercalation compounds.[44] Many Li and Na intercalation compounds, used as electrodes in Li and Na batteries for example, also have a layered crystal structure with two-dimensional triangular interstitial sublattices that can accommodate guest species. In this context, the ordered $ZrO_{1/6}$ phase, where oxygen selectively fills alternating interstitial layers of the hcp crystal structure, can be viewed as a staged compound, as is observed in Li_xC_6, Li_xTiS_2, and Li_xCoO_2.

During oxidation of Zr, oxygen diffuses in from the surface, and the oxygen chemical potential decreases from a high at the surface, to a low in the interior. Across this chemical potential gradient the stable phases vary accordingly, as depicted schematically in Fig. 12. Experimentally,[45,46] it is found that α-ZrO_2 is the dominant phase at the surface, and a mix of mostly α-ZrO_2 and β-ZrO_2 forms at the metal-oxide interface. The stability of β-ZrO_2 is usually explained by the large compressive stress at the metal-oxide interface due to the volume expansion associated with oxidation. Just below the metal-oxide interface oxygen-rich metal grains are observed,[46,47] which correspond to the ordered oxygen interstitial phases. All suboxides, including δ'-ZrO are predicted to be metallic with a sizable density of states at the Fermi level. This has consequences for the oxidation kinetics, as the ingress of oxygen is not limited by electron transport. Due to the metallic nature of the suboxides, oxygen diffusion through the suboxides can be described by simple Fickian diffusion kinetics. The rate at which oxygen can be incorporated into α-Zr is important for determining the overall rate of oxidation, and the structure of the ordered phases are likely to play an important role in determining the diffusion rate. The $ZrO_{1/6}$ structure has open layers that may provide easy pathways for oxygen diffusion, while the $ZrO_{1/3}$ and $ZrO_{1/2}$ lack any pathways that appear to be as favorable.

V. CONCLUSIONS

In conclusion, the main results of this study are (1) the prediction of a hexagonal 0-K ground-state structure of stoichiometry ZrO; (2) a cluster Hamiltonian which predicts that there exist 0-K ground-state oxygen orderings in α-Zr at composition $ZrO_{1/6}$, $ZrO_{2/9}$, $ZrO_{1/4}$, $ZrO_{1/3}$, $ZrO_{4/9}$- and $ZrO_{1/2}$, and predicts that there exist an infinite number of possible stacking sequences which lie on the convex hull between these ground states; (3) a description of the order/disorder transitions in $ZrO_{1/2}$ and in the composition range between $ZrO_{1/6}$ and $ZrO_{1/3}$; (4) construction of a temperature-composition phase diagram for ZrO_x in the range $0 \leqslant x \leqslant 2$ at low temperature.

ACKNOWLEDGMENTS

This work was supported by the Consortium for Advanced Simulation of Light Water Reactors (http://www.casl.gov), an Energy Innovation Hub (http://www.energy.gov/hubs) for Modeling and Simulation of Nuclear Reactors under U.S. Department of Energy Contract No. DE-AC05-00OR22725. First principles calculations were performed using computational resources provided under allocation No. TG-DMR100093 on Extreme Science and Engineering Discovery Environment (XSEDE), which is supported by National Science Foundation Grant Number OCI-1053575.

*bpuchala@umich.edu
†avdv@engineering.ucsb.edu

[1] A. Atkinson, Rev. Mod. Phys. **57**, 437 (1985).
[2] J. P. Abriata, J. Garcés, and R. Versaci, Bull. Alloy Phase Diagrams **7**, 116 (1986).
[3] P. Bouvier, E. Djurado, G. Lucazeau, and T. Le Bihan, Phys. Rev. B **62**, 8731 (2000).
[4] J. L. Murray and H. A. Wriedt, Bull. Alloy Phase Diagrams **8**, 148 (1987).
[5] M. Hirabayashi, S. Yamaguchi, and T. Arai, J. Phys. Soc. Jpn. **35**, 473 (1973).
[6] T. Arai and M. Hirabayashi, J. Less-Common Met. **44**, 291 (1976).
[7] R. Arroyave, L. Kaufman, and T. W. Eager, Calphad **26**, 95 (2002).
[8] Y.-J. Hao, L. Zhang, X.-R. Chen, L.-C. Cai, Q. Wu, and D. Alfè, Phys. Rev. B **78**, 134101 (2008).
[9] G. Fadda, L. Colombo, and G. Zanzotto, Phys. Rev. B **79**, 214102 (2009).
[10] X. Zhao and D. Vanderbilt, Phys. Rev. B **65**, 075105 (2002).
[11] A. V. Ruban, V. I. Baykov, B. Johansson, V. V. Dmitriev, and M. S. Blanter, Phys. Rev. B **82**, 134110 (2010).

[12]B. P. Burton, A. van de Walle, and H. T. Stokes, J. Phys. Soc. Jpn. **81**, 014004 (2012).
[13]N. Ni, S. Lozano-Perez, J. Sykes, and C. Grovenor, Ultramicroscopy **111**, 123 (2011).
[14]N. Ni, D. Hudson, J. Wei, P. Wang, S. Lozano-Perez, G. D. W. Smith, J. M. Sykes, S. S. Yardley, K. L. Moore, S. Lyon, R. Cottis, M. Preuss, and C. R. M. Grovenor, Acta Mater. **60**, 7132 (2012).
[15]Y. Dong, A. T. Motta, and E. A. Marquis, J. Nucl. Mater. (2013), doi:10.1016/j.jnucmat.2013.08.055.
[16]R. T. Downs and M. Hall-Wallace, Am. Mineral. **88**, 247 (2003).
[17]G. Bergerhoff and I. D. Brown, in *Crystallographic Databases*, edited by F. H. Allen *et al*. (Hrsg.) (Chester, International Union of Crystallography, 1987).
[18]G. Sethi, P. Sunal, M. W. Horn, and M. T. Lanagan, J. Vac. Sci. Technol., A **27**, 577 (2009).
[19]S. Andersson, Acta Chem. Scan. **13**, 415 (1959).
[20]C. Jiang, C. R. Stanek, N. A. Marks, K. E. Sickafus, and B. P. Uberuaga, Philos. Mag. Lett. **90**, 435 (2010).
[21]P. Hohenberg and W. Kohn, Phys. Rev. **136**, B864 (1964).
[22]G. Kresse and J. Hafner, Phys. Rev. B **47**, 558 (1993).
[23]G. Kresse and J. Hafner, Phys. Rev. B **49**, 14251 (1994).
[24]G. Kresse and J. Furthmller, Comput. Mater. Sci. **6**, 15 (1996).
[25]G. Kresse and J. Furthmuller, Phys. Rev. B **54**, 11169 (1996).
[26]G. Kresse and D. Joubert, Phys. Rev. B **59**, 1758 (1999).
[27]J. P. Perdew, K. Burke, and M. Ernzerhof, Phys. Rev. Lett. **77**, 3865 (1996).
[28]J. P. Perdew, K. Burke, and M. Ernzerhof, Phys. Rev. Lett. **78**, 1396 (1997).
[29]J. M. Sanchez, F. Ducastelle, and D. Gratias, Physica A **128**, 334 (1984).
[30]See Supplemental Material at http://link.aps.org/supplemental/10.1103/PhysRevB.88.094108 for methodological details and additional analysis.
[31]G. L. W. Hart, V. Blum, M. J. Walorski, and A. Zunger, Nat. Mater. **4**, 391 (2005).
[32]L. J. Nelson, G. L. W. Hart, F. Zhou, and V. Ozoliņš, Phys. Rev. B **87**, 035125 (2013).
[33]A. van de Walle and M. Asta, Model. Simul. Mater. Sci. Eng. **10**, 521 (2002).
[34]A. Kohan, P. Tepesch, G. Ceder, and C. Wolverton, Comput. Mater. Sci. **9**, 389 (1998).
[35]D. de Fontaine, G. Ceder, and M. Asta, Nature (London) **343**, 544 (1990).
[36]M. Hirabayashi, S. Yamaguchi, T. Arai, H. Asano, and S. Hashimoto, Phys. Status Solidi A **23**, 331 (1974).
[37]W. A. Harrison, *Electronic Structure and the Properties of Solids* (Dover, Mineola, NY, 1989).
[38]K.-H. Xue, P. Blaise, L. R. C. Fonseca, and Y. Nishi, Phys. Rev. Lett. **110**, 065502 (2013).
[39]Y.-L. Lee, J. Kleis, J. Rossmeisl, and D. Morgan, Phys. Rev. B **80**, 224101 (2009).
[40]L. Wang, T. Maxisch, and G. Ceder, Phys. Rev. B **73**, 195107 (2006).
[41]T. Nagase, B. Puchala, and A. Van der Ven (unpublished).
[42]B. P. Burton and A. van de Walle, Calphad **39**, 97 (2012).
[43]B. P. Burton and A. van de Walle, Calphad **37**, 151 (2012).
[44]A. Van der Ven, B. Puchala, and T. Nagase, J. Power Sources **242**, 400 (2013).
[45]N. Pétigny, P. Barberis, C. Lemaignan, C. Valot, and M. Lallemant, J. Nucl. Mater. **280**, 318 (2000).
[46]A. Yilmazbayhan, E. Breval, A. T. Motta, and R. J. Comstock, J. Nucl. Mater. **349**, 265 (2006).
[47]A. T. Motta, A. Yilmazbayhan, R. J. Comstock, J. Partezana, G. P. Sabol, B. Lai, and Z. Cai, J. ASTM Int. **2**, 12375 (2005).